Halloysite nanotube@N-doped graphene heterostructure enabled advanced potassium ion hybrid capacitor anode

Yongrong Sun [a], Jiefeng Zheng [b], Fayong Li [a], Yuanhui Long [b], Dong Xie [a,*], Hongyan Li [b,*], Mingxian Liu [b,*]

[a] Biomaterials Engineering Technology Research Center, Institute of Biological and Medical Engineering, Guangdong Academy of Sciences, Guangzhou 510316, China
[b] Department of Materials Science and Engineering, College of Chemistry and Materials Science, Jinan University, Guangzhou 511443, China

ARTICLE INFO

ABSTRACT

Graphene is considered one of the most promising candidates for potassium ion hybrid capacitor (PIHC) anode due to its excellent electrical conductivity and short ion diffusion pathway. However, the relatively weak adsorption ability for potassium ion (K^+) and poor K-storage ability of graphene hinder further large-scale application. Herein, a three-dimension electronic modulation strategy is proposed to introduce the electron deficient in graphene by fabricating a stable heterostructure with wrapping nitrogen-doped graphene (NG) on halloysite nanotube (HNTs) noted as HNTs@NG. The electronic structure of graphene is modulated in two-dimension (2D) plane direction through doping N atoms and perpendicular to 2D plane through forming co-valent bonds between carbon atoms and oxygen atoms. The graphene with fine-regulated electronic structure delivers a high rate capability (387.1 mA h g^{-1} at 0.05 A g^{-1}) and good capacity retention (105.8 mA h g^{-1} at 1.0 A g^{-1} over 2000 cycles) of HNTs@NG, and further insures energy density and cycle stability of as-developed PIHC. This finding offers an effective way to modulate electron structure of graphene to achieve the development advanced PIHC.

1. Introduction

Potassium ion batteries (PIBs) have attracted extensive attention and been considered as a promising next-generation energy storage system, owing to the abundant resource of potassium, high economic efficiency and theoretical energy density [1–3]. Taking into account of the demand for high power density, high energy density and long cycling life, potassium ion hybrid capacitor (PIHC) with a battery-type material as anode and a capacitor-type material as cathode has been taken as an ideal configuration for potassium ion power source in recent years [4]. As yet, the performance of PIHC in practical application is mainly plagued by battery-type anode materials in terms of poor rate performance, sluggish kinetics and large volume variations owing to large radius of potassium ion (K^+1.38 Å) [5,6]. In consequence, it is critical for developing battery-type anode materials to achieve high performance of PIHC.

In past years, anode materials with variety of dimensions for PIHC mainly derive from existing -PIBs anodes, such as carbon fiber [7], carbon nanotubes [8], graphene [9], MoS$_2$ [10], and three-dimension

(3D) carbon [11,12]. Among them, graphene has been regarded as one of the most promising anode materials owing to its short K^+ diffusion pathway aroused by the unique two-dimension (2D) structure [13–15]. Unfortunately, pristine graphene composed of intact hexagonal carbon ring as building blocks confines the K^+ diffusion and K-storage in spaces paralleled to 2D plane due to the high energy barrier of basal plane and weak binding between potassium and graphene [16, 17]. Considering the strong electron donating ability of K atom, heteroatom doping to fabricate electron deficiency of active site has been proposed as an effective strategy to modify the surface property of graphene [18,19]. It has been verified that the electronic structure is tailored after introducing heteroatoms (N, B, P, F, S) by breaking intact hexagonal carbon ring in graphene networks [20–25]. Among these heteroatoms, nitrogen (N) has been widely selected as doping atoms for graphene due to its high electronegativity and similar radius with carbon. It has demonstrated that N-doped few layer graphene can achieve high K-storage capacity due to increment number of storage sites [26]. Great efforts have been verified that the interaction between the K^+ and N-doped graphene is stronger than that between the K^+ and pristine

graphene owing to the electron affinities of N atoms, which is beneficial to K^+ diffusion and eventually accelerates the electrochemical kinetics [27–30]. Furthermore, replacing C atoms with N atoms can induce electron deficiency in adjacent C atoms, making them favorable sites for K-storage. Although N-doping has improved the K^+ diffusion and K-storage ability of graphene, the electrochemical performance is still unsatisfying. Exploring a new strategy to further boost the performance of graphene in terms of K^+ diffusion and K-storage is still a great challenge.

To further introduce the electron deficient state of active sites in graphene, we propose a 3D electron regulation strategy that not only tailors the electronic structure of active sites in the 2D plane of graphene by doping N atoms, but also affects the electronic structure of active sites in perpendicular direction to 2D plane of graphene by forming covalent bonds between carbon atoms and high electronegativity oxygen atoms. To adjust the electronic structure in perpendicular direction to 2D plane of graphene, we fabricate a heterostructure with interfacial covalent bonds for PIHC anode by wrapping nitrogen-doped graphene (NG) on halloysite nanotube (HNTs) by *in-situ* chemical vapor deposition (CVD) noted as HNTs@NG, in which a large number of oxygen atoms on outer surface of HNTs can achieve the electronic modulation from carbon to oxygen through interfacial covalent bonds [31–34]. A series of physical characterization methods and electrochemical measurements are used to elucidate the influence mechanism of the surface electronic property of graphene on K^+ diffusion and K-storage. This electronic modulated strategy provides a novel method to modify the property of active sites and also opens up an avenue for achieving the high performance for advanced PIHC anode.

2. Experimental

2.1. Preparation of materials

The sample of HNTs@NG heterostructure was prepared by CVD method with triethylamine as carbon and nitrogen precursor. The CVD setup was mainly composed of a horizontal tube furnace and an importing system. Briefly, HNTs (1.0 g) powder was put into quartz boats and placed in the center of a quartz tube. High purity argon gas was introduced into the tube furnace at gas-flow of 500 mL min^{-1} during the elevated temperature process (5 °C min^{-1}). When the targeted temperature (900 °C) was reached, the pure argon gas was re-routed a gas bottle with triethylamine (by bubbling argon gas through liquid triethylamine at gas-flow of 1.0 L min^{-1}). After maintaining for 90 min, the argon/triethylamine mixed flow was shut off and followed by cooling down naturally to room temperature in flowing pure argon. After this process, black solid was obtained with NG layers formed over the HNTs surface possessing strong interfacial covalent bonds, as HNTs@NG. In addition, the obtained HNTs@NG powder was treated with concentrated hydrochloric acid (HCl) and hydrofluoric acid (HF) to dissolve the HNTs in order to obtain hollow nitrogen-doped graphene shell, as NG shell. In a typical procedure, HNTs@NG (1.0 g) was dispersed into HCl (20 mL) under stirring condition. After stirred for 2 h, the obtained suspension was washed for three times. The collected solid was dissolved into HF (20 mL) with continuously stirred for 2 h, then washed by distilled water for several times until the supernatants achieved pH=7 and dried at 80 °C. The reference sample of graphene (G) shell was prepared by similar method except that triethylamine was replaced by ethanol.
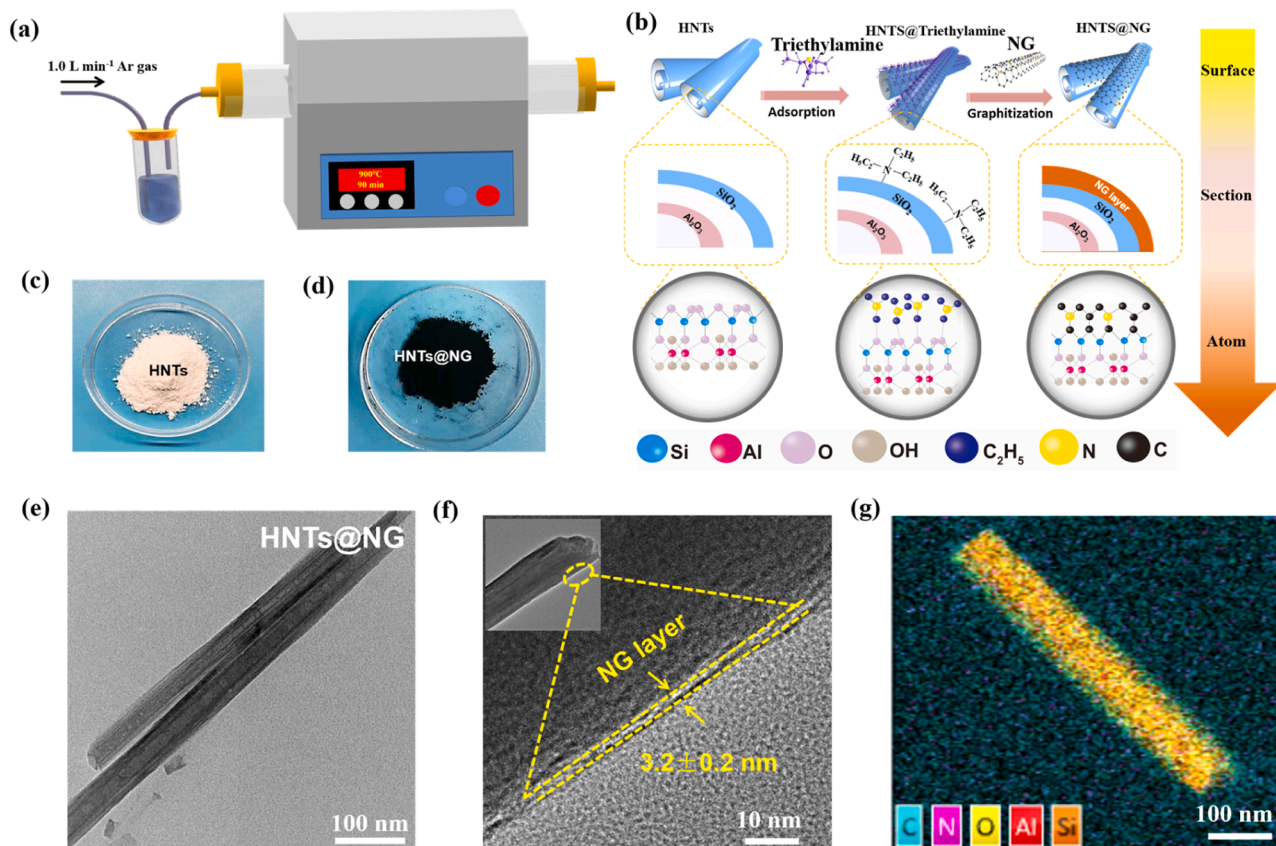

Fig. 1. (a) and (b) Schematic diagram of the preparation process and interfacial structure of HNTs@NG heterostructure, photographs of (c) HNTs and (d) HNTs@NG, (e) TEM image of HNTs@NG, (f) HR-TEM image of HNTs@NG, and (g) elemental mapping of HNTs@NG.
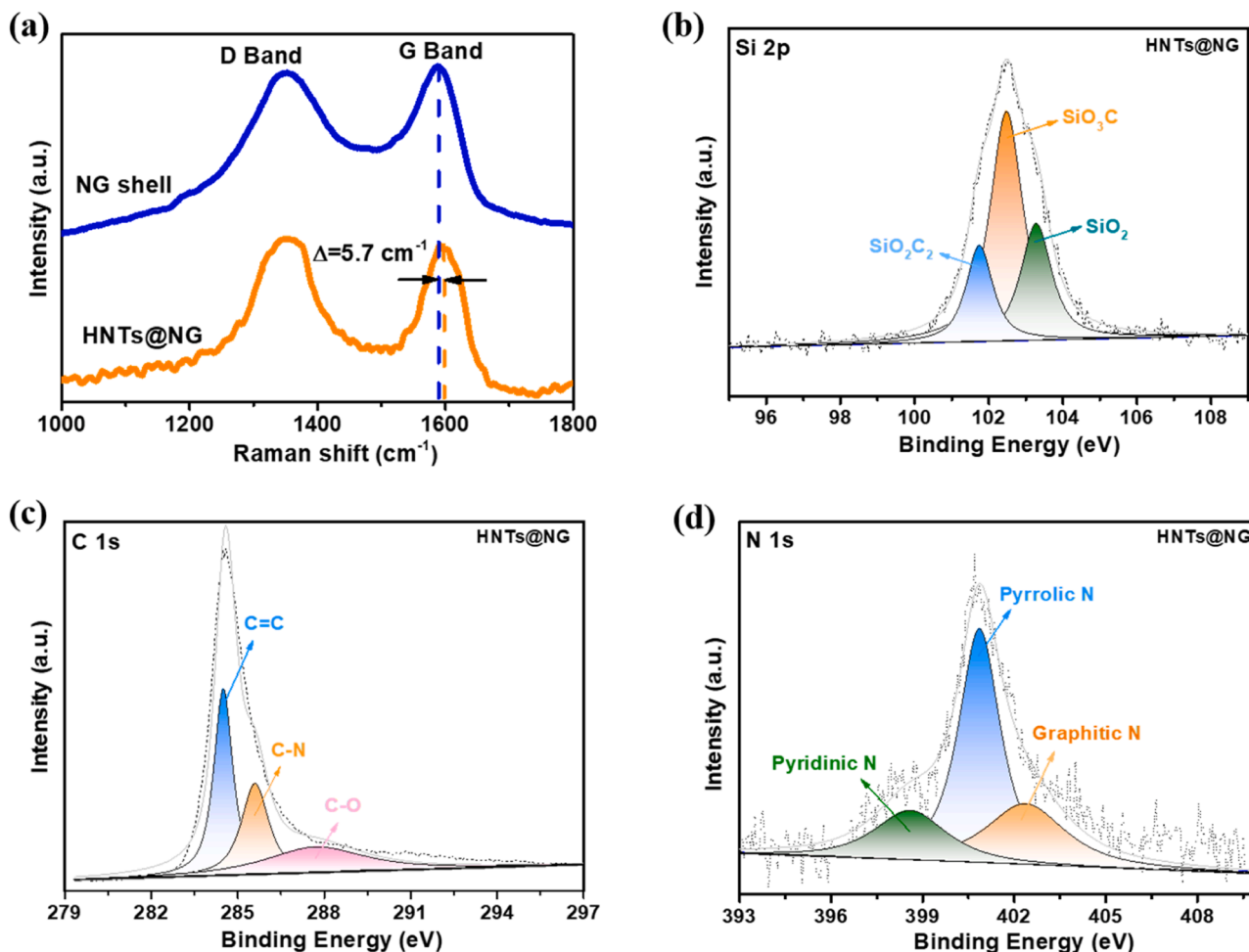
Fig. 2. Chemical composition of HNTs@NG. (a) Enlarged Raman spectra for HNTs@NG and NG shell, (b) XPS of high-resolution Si 2p core level, (c) C 1s core level, (d) N 1s core level of HNTs@NG.

2.2. Physical characterizations

The characteristic of microstructure and element distribution were examined by scanning electron microscopy (SEM) (ZEISS Sigma 500, UK) and transmission electron microscopy (TEM) (2100F, JEOL Ltd., Japan). Raman spectroscopy was collected on Lab RAM HR800 (Horiba Jobin-Yvon LabRAM HR800, France) at room temperature (excitation wavelength of 532 nm). The chemical composition and chemical bonding state were analyzed by X-ray photoelectron spectroscopy (XPS) (ESCALAB250Xi, Thermo Fisher Scientific Ltd., USA). The Thermo gravimetric (TG) curves were obtained TG analyzer (TGA2, METTLER TOLEDO Co. Ltd., Switzerland) from 50 °C to 900 °C with a ramping rate of 10 °C min^{-1}.

2.3. Electrochemical measurements

All the performance tests were employed with coin type cells (CR2032). The active material (HNTs@NG, HNTs, NG shell and G shell) was mixed with conductive material and binder (sodium carboxymethyl cellulose, CMC) with a mass ratio of 8:1:1 and cast on a copper foil current collector. Potassium metal was adopted as the counter and reference electrodes in half-cell. 0.8 M of KPF$_6$ in ethylene carbonate (EC) and diethyl carbonate (DEC) with a volume ratio of 1:1 and glass fiber act as electrolyte and separator, respectively. Before assembling the PIHC using HNTs@NG as anode and active carbon (AC) as cathode, cyclic voltammetry (CV) curves of HNTs@NG and AC (mass ratio of 1:2) were carried out using CHI 760 Electrochemical Workstation at sweep

rate of 1.0 mV s^{-1}, respectively. The PIHC was assembled with HNTs@NG as anode and AC as cathode (mass ratio of 1:2) (denoted as HNTs@NG//AC). Galvanostatic charge-discharge (GCD) measurements were conducted on LAND-CT200A instrument. CV curves and electrochemical impedance spectroscopy (EIS) were conducted out using CHI 760 Electrochemical Workstation at various scan rates (0.1 to 1.0 mV s^{-1}) and frequencies (0.01 Hz to 100 kHz).

The proportion of capacitance-controlled and diffusion-controlled processes can be calculated by the mathematical correlation between measured peak current (i) and the sweep rate (υ) according to the following Equation [35]:

$$i = a\nu^b \tag{1}$$

where the values of a and b derive from the intercept and the gradient of the linear relation of $\log(i)$ vs. $\log(\nu)$.

The relative contribution from capacitance-controlled and diffusion-controlled can be clarified by using the following Equation [36]:

$$i = k_1\nu + k_2\nu^{1/2} \tag{2}$$

or

$$i/\nu^{1/2} = k_1\nu^{1/2} + k_2 \tag{3}$$

The specific K^+ diffusion coefficients (D_K) is calculated using the standard approach based on Equation [37]:

$$D_K = [4 / (\pi\tau)] \times [(m_B V_M)/(M_b S)]^2 \times (\Delta E_s/\Delta E_\tau)^2 \tag{4}$$
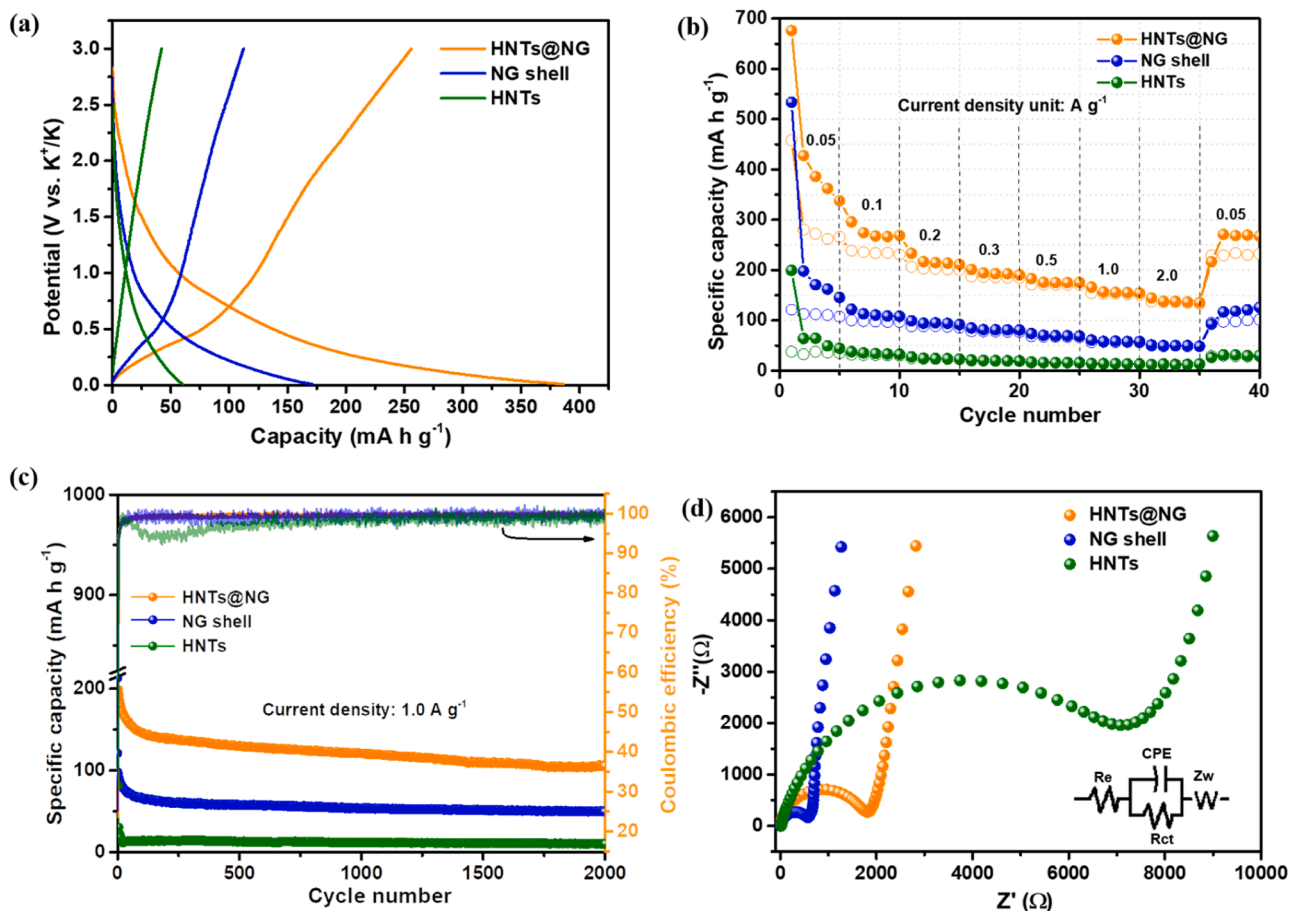
Fig. 3. Electrochemical performance of HNTs@NG, HNTs and NG shell as potassium ion battery anode in half-cell. (a) GCD curves of HNTs@NG, NG shell and HNTs at 0.05 A g^{-1}, (b) rate performance, (c) long-term cycling performance under current densities of 1.0 A g^{-1} and (d) EIS curves of HNTs@NG, HNTs and NG shell.

where τ, m_{B}, S, V_{M}, and M_{b} stand for the galvanostatic current pulse time, mass of the active materials, geometric area of the electrode, molar volume and molar mass of active material, respectively.

The energy density and power density (E, Wh kg^{-1} and P, W kg^{-1}) of HNTs@NG//AC were calculated according to GCD curves and the equation: $E = \int VdQ$, where E, V and Q are energy density, voltage, and capacity, respectively; $P = E/t$, P is power density and t is discharging time.

3. Results and discussion

In order to fabricate the stable heterostructure, HNTs@NG was prepared using triethylamine as carbon and nitrogen precursor through a one-step CVD, as illustrated in Fig. 1a. With bubbling argon gas through liquid triethylamine, the triethylamine is poured into a tube furnace and rapidly adsorbs onto the external surface of HNTs by electrostatic adsorption effect. Subsequently, the adsorbed triethylamine decomposes into small fragments of containing carbon and nitrogen species. With the reaction proceeding, these tiny fragments *in-situ* graphitize into NG layer on the surface of HNTs to finally generate the durable heterogeneous structure with forming covalent bonds (Fig. 1b). After exposing in triethylamine vapor at optimal 900 °C for 90 min, the initial white powder (Fig. 1c) turns into black (Fig. 1d). SEM and TEM display that the pristine HNTs (Figs. S1 and S2) owns typical 1D hollow tubular morphology with smooth and sharp surface.

In order to identify the interface structure, HNTs@NG was characterized by HR-TEM. Compared with pristine HNTs, it is difficult to present the inner diameter of HNTs after introducing NG layer, because the NG has a tendency to grow onto/into the HNTs outer/inner surface.

Therefore, the surface of HNTs@NG becomes coarseness in Fig. 1e and the thickness of NG layer is about 3.2 ± 0.2 nm (Fig. 1f). The large inner diameter of HNTs (about 30 nm) allows the deposition of carbon in the interior of HNTs. But, comparing with inner surface, carbon could be more likely to be deposited on the external surface of HNTs and form Si-O-C covalent bonds due to steric hindrance of inner diameter. The elements of HNTs@NG heterostructure including C, N, O, Si, Al are uniformly distributed throughout the whole nanotube as indicated in Figs. 1g and S3. According to the TG curves (Fig. S4), it can be speculated that the NG layer mass is 8.1 wt.%. According to above results, HNTs@NG heterostructure has been successfully prepared.

To analyze the crystal structure and local carbon structure evolution, XRD patterns and Raman spectra were carried out. The HNTs exhibits characteristic peaks at 12.2°, 20.1°, 24.7°, and 35.0° (Fig. S5), which are well assigned to the (001), (020, 110), (002) and (200, 130) planes, respectively. Comparing with raw HNTs, HNTs after 900 °C thermal treatment (HNTs-900 °C) exhibited only a broadened diffraction peak at 23.2°, which could be attributed to the formation of amorphous product (metahalloysite) through dehydroxylation and the dissociative amorphous SiO$_2$ [38]. HNTs@NG exhibits a characteristic peak similar to that of HNTs-900 °C, which is assigned to amorphous product of HNTs and (002) plane of graphitic carbon [39]. The calculated value of I$_D$/I$_G$ ratio is about 1.04 in Raman spectra (2a), which is higher than that of NG shell (0.98) prepared under the same condition, confirming that the introduction of HNTs leads to a higher degree of defective sp^3 carbon. Generally, thin carbon layers display 2D characteristic peak at ~2670 cm^{-1} in Raman spectrum and few layer in TEM image are often recognized as graphene [40]. D band (1346 cm^{-1}), G band (1580 cm^{-1}) and 2D band (2674 cm^{-1}) in the intrinsic Raman features of graphene in this
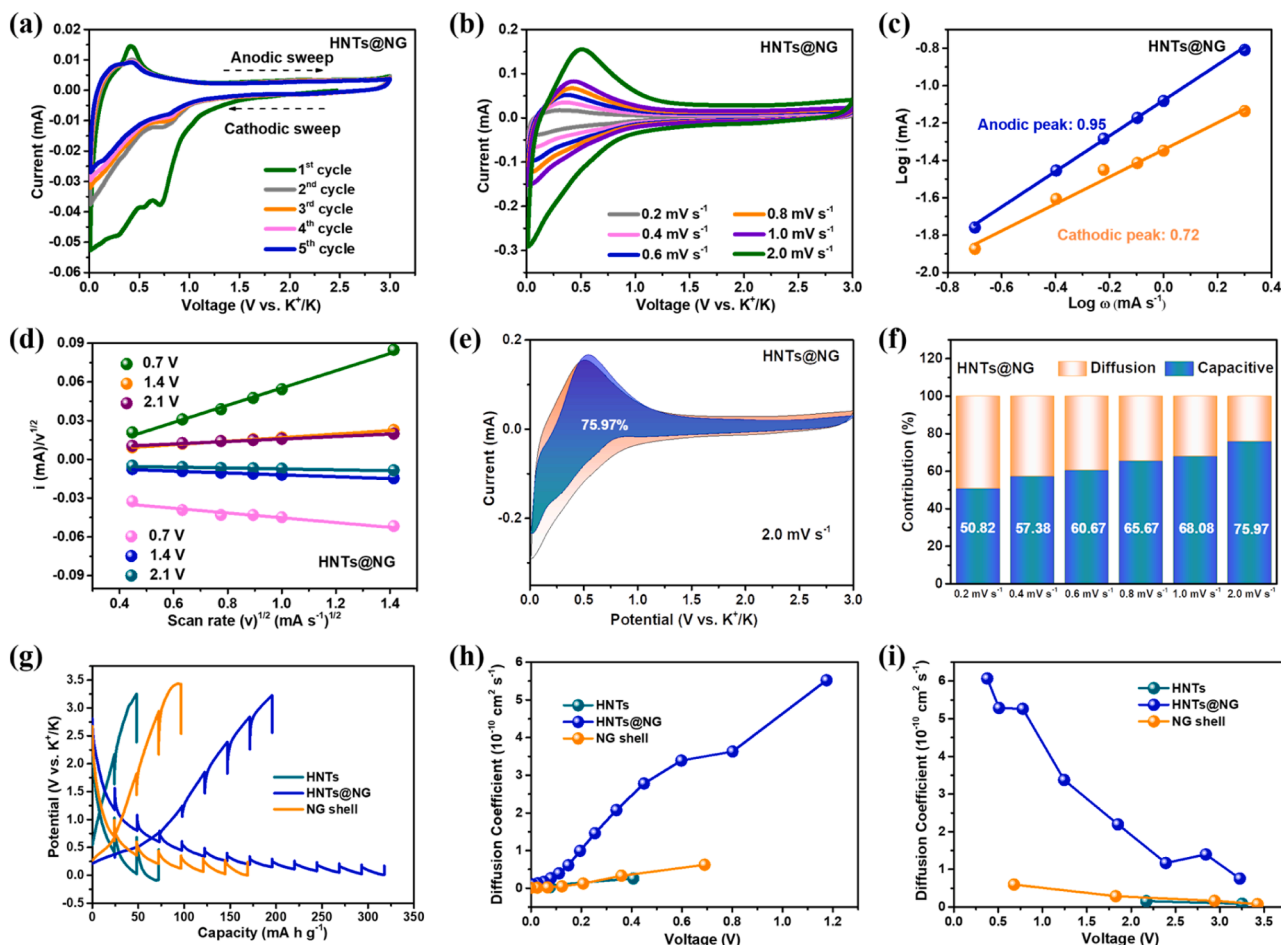
Fig. 4. Analysis of K^+ kinetics of HNTs@NG. (a) CV curves with various cycles at 0.1 mV s^{-1}, (b) CV curves with different sweep rate, (c) the relationship of log (i) vs. log(ω), (d) correlation of i/$\nu^{1/2}$ vs. $\nu^{1/2}$, (e) the capacitive-controlled contributions at 2.0 mV s^{-1}, (f) bar graph of contribution ratios, (g) GITT curves, (h) and (i) diffusion coefficients of K^+ (D$_k$) at different voltage during charge and discharge for HNTs@NG, HNTs and NG shell.

work are detected (Fig. S6). So, the formed carbon layer on HNTs was named as graphene. Meanwhile, significant Raman shift is observed, that the G band peak of HNTs@NG positively shifts by positively shifts by 5.7 cm^{-1} in Fig. 2a. This shift indicates the electronic structure rearrangement of carbon arises from charge transfer between two lone-pair electron in oxygen atoms on HNTs surface and carbon [27].

The covalent interfacial framework between HNTs and NG layer was further analyzed by XPS measurement. XPS spectra display distinct characteristic peaks of Si, C, Al, O and N, which directly proves the coexistence of them on HNTs@NG (Fig. S7). In the characteristic peaks of Si 2p (Fig. 2b), except for the typical peak of SiO$_2$ at 103.4 eV, the peaks located at 101.6 eV and 102.5 eV can be corresponded to SiO$_2$C$_2$ and SiO$_3$C, respectively, [41] which can prove the formation of stable covalent interfacial framework between HNTs and NG layer. In high-resolution C 1s core level of HNTs@NG displays (Fig. 2c) obvious C = C, C-N and C-O peaks [42]. The N 1s core level of characteristic peaks including pyridinic N, pyrrolic N and graphitic N [43] can be presented in Fig. 2d. Depending on these results, stable heterostructure composed by NG layer and HNTs are successfully fabricated by forming Si-O-C-N interfacial covalent bonds through one-step CVD method.

In order to estimate the effect of heterostructure between HNTs and NG layer on electrochemical performance, samples of HNTs, NG shell and G shell were selected as reference groups. Compared with HNTs@NG (Fig. 3), NG shell and G shell (Fig. S8), the specific capacity, rate and stability of HNTs are negligible, which eliminates the effect of HNTs on electrochemical performance. The achieved specific capacity of HNTs@NG (387.1 mA h g^{-1}) is markedly superior to the samples of NG

shell (171.8 mA h g^{-1}) and G shell (76.2 mA h g^{-1}(Fig. S8a). Even at a high current density of 2.0 A g^{-1} and restored to 0.05 A g^{-1}, the HNTs@NG retains a high reversible capacity of 138.0 and 268.6 mAh g^{-1}, respectively (Fig. 3b), relative to NG shell and G shell (Fig. S8b). Over 2000 cycles at 1.0 A g^{-1}, the specific capacity of HNTs@NG (105.8 mA h g^{-1}) maintains 2.2-fold and 4.5-fold higher than that of NG shell and G shell, respectively (Figs. 3c and S8c). In further contexts, the long-term cyclic performances of HNTs@NG at various current densities are complements in Fig. S9. These results confirm that the interfacial co-valent bonds can promote the K-storage ability and long-term cycling stability, which will be discussed detail in the next section. The smaller semicircle at high frequency region of HNTs@NG than that of HNTs represents the low charge transfer resistance because of presence of NG layer on HNTs (Fig. 3d).

The origin of superior electrochemical performance of hetero-structure is further comprehended by the analysis of K^+ kinetics. In Fig. 4a, an irreversible reduction peak of HNTs@NG at the first cycle can be observed, mainly assigned to the formation of solid electrolyte interface (SEI). There is no detectable shape difference between the fourth and fifth curves, indicating the remarkable reversibility of HNTs@NG. The same phenomenon occurs in NG shell (Fig. S10) and HNTs (Fig. S11), suggesting that storage mechanism is not changed after introduction of heterostructure.

As is well known, insertion and adsorption mechanisms play important role in K-storage process. The adsorption mechanism is often termed as capacitive-controlled mechanism, which can promote rapid ion diffusion and maintain excellent structure stability. According to CV
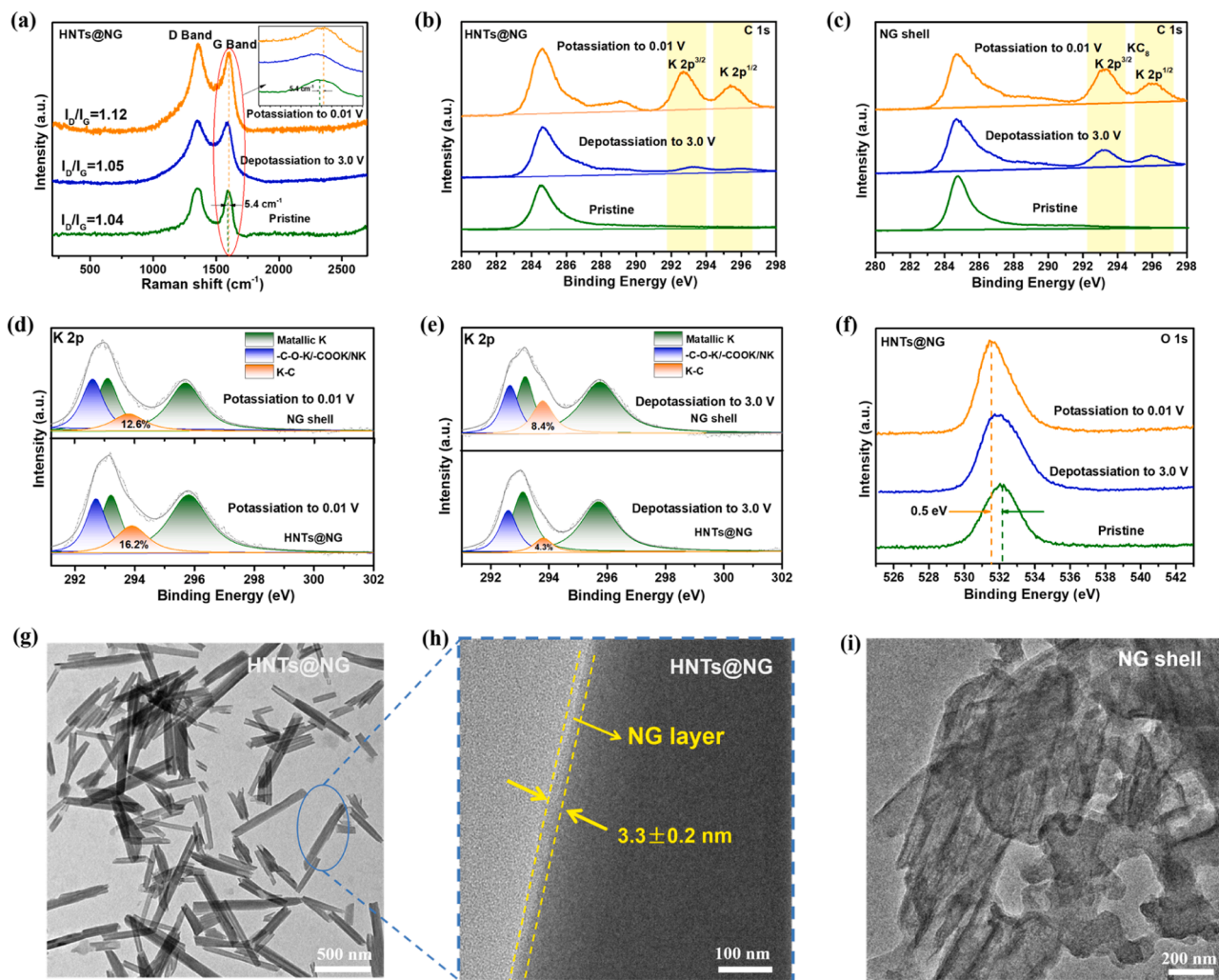
Fig. 5. Analysis on the K-storage mechanism of HNTs@NG. (a) Ex-situ Raman spectra of HNTs@NG, ex-situ C 1s of (b) HNTs@NG and (c) NG shell, ex-situ K 2p of (d) potassiation/(e) depotassiation for HNTs@NG and NG shell, (f) O 1s of HNTs@NG under potassiation/depotassiation, (g) ex-situ TEM and (h) HR-TEM of HNTs@NG, (i) ex-situ TEM for NG shell under potassiation/depotassiation at 1.0 A g^{-1}.

curve (Fig. 4b) and Eq. (1), b values of HNTs@NG are 0.95 and 0.72 for anodic oxidation and cathodic reduction, respectively (Fig. 4c). Compared with NG shell (Fig. S10) and HNTs (Fig. S11), the b values of HNTs@NG are more closed to 1, suggesting that capacitive-controlled mechanism dominates the K-storage after introduction of heterostructure.

The capacitive-controlled (k_1v) and diffusion-controlled ($k_2v^{1/2}$) can be quantified by CV curves (Fig. 4b) and Eq. (2). The values of k_1 and k_2 are attained in Fig. 4d based on fitting CV curves with various scan rates and the Eq. (3). The capacitive-controlled contribution of HNTs@NG surprisingly reaches 75.97% at 2.0 mV s^{-1} in Fig. 4e. Comparatively speaking, the contribution ratios of capacitive-controlled of HNTs@NG (Fig. S12) are higher than those of NG shell (Fig. S13) and HNTs (Fig. S14). Dramatically enhanced the percentage of capacitive-controlled contributions of HNTs@NG with increasing sweep rate (Fig. 4f) further validates that K-storage process conforms to capacitive-controlled demonstrating satisfying electrochemical performance. The K^+ transport kinetics of HNTs@NG was clarified by Galvanostatic Intermittent Titration Technique (GITT). HNTs@NG (Fig. 4g, h and i) exhibits high D_K for both the charge and discharge processes as compared to those of NG shell and HNTs, indicating K^+ diffusion in the heterostructure being kinetically favorable.

To unravel the nature of achieved electrochemical behavior of heterostructure, the structural evolution of HNTs@NG during potassiation/

depotassiation process was carried out via ex-situ Raman spectrum. Fig. 5a shows the Raman spectra of HNTs@NG during potassiation/depotassiation process with the range of 0.01–3.0 V. Upon potassiation, the calculated I_D/I_G ratio of HNTs@NG shows an increase from 1.04 (pristine) to 1.12 along with a positively shift, indicating to ascendant disordered caused by K^+ adsorption [44,45]. Subsequently, the I_D/I_G value returns to 1.05 closed to pristine value after the depotassiation, showing a reversible variation.

Ex-situ XPS was carried out to explore the relationship between K^+ adsorption/K-storage and active site of heterostructure after potassiation/ depotassiation process. As active sites, in high-resolution spectra of C 1s (Fig. 5b and c), the obvious K 2p$^{3/2}$ and K 2p$^{1/2}$ peaks can be appeared for HNTs@NG and NG shell after potassiation status, indicating the strong interaction between K^+ and carbon due to doping N atom into graphene. Compared with K 2p of NG shell in Fig. 5d, the K-C peak intensity of HNTs@NG (Fig. 5e) increase significantly after potassiation, and then decrease sharply in the subsequent depotassiation process. This demonstrates that HNTs@NG owns strong K adsorption/ desorption ability, which is crucial for the improvement of capacity and cyclability.

Based on the consensus that adsorption/desorption is closely related to the electronic structure of active sites, we examine the effect of interfacial covalent bonds to electronic structure of NG active sites, especially the O 1s and Si 2p of interfacial covalent bonds to probe the
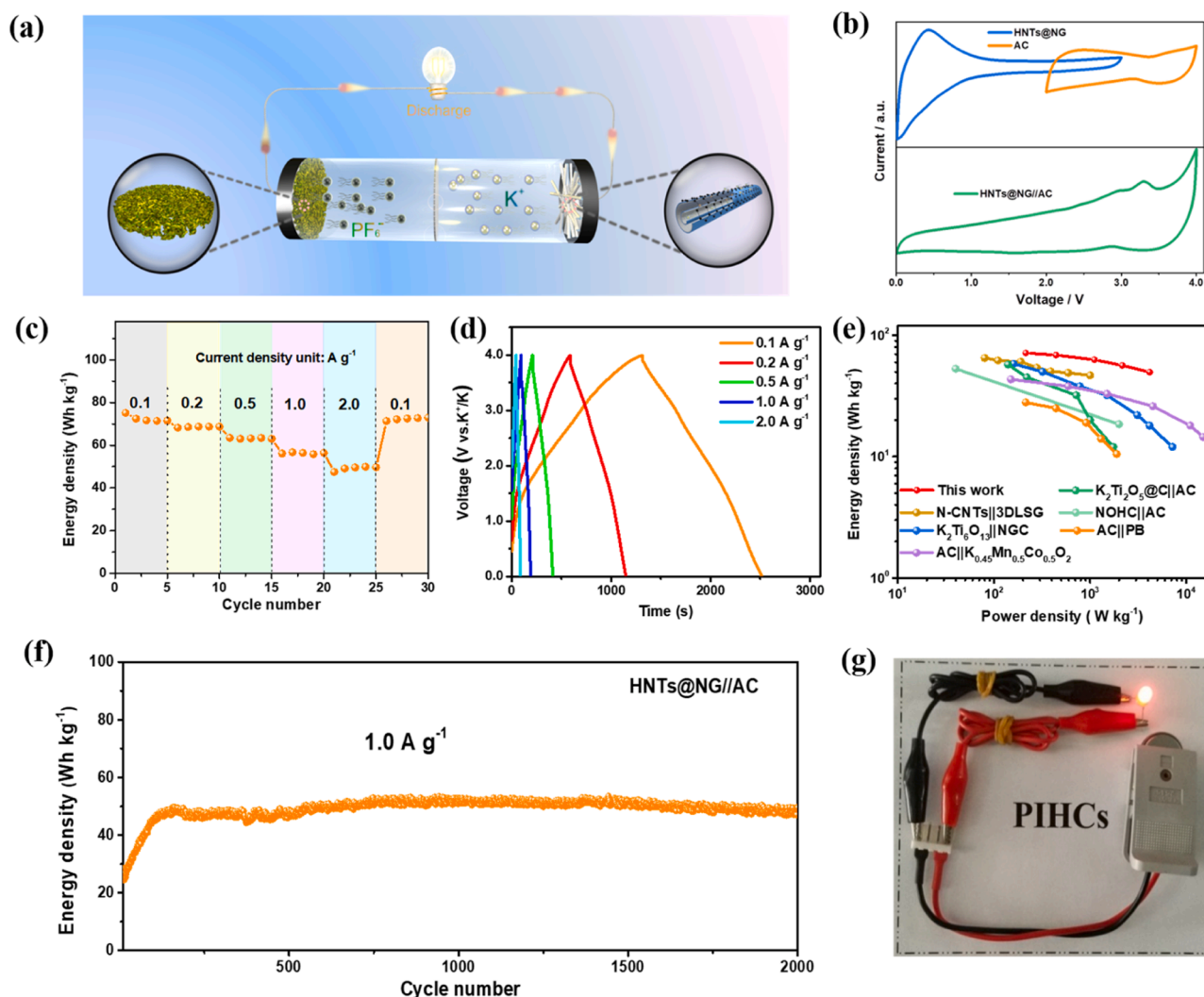
Fig. 6. Electrochemical behavior of PIHC with HNTs@NG as anode. (a) Schematic diagram of the PIHC, (b) CV curves of half-cell (top) and PIHC (bottom), (c) rate capability and (d) GCD curves at various current densities, (e) ragone plots in comparison with PIHC in previously reported literatures, (f) long life cycle curves of PIHC device at 1.0 A g^{-1}, (g) digital photo of LED by our hybrid capacitor device.

nature of K^+ diffusion and K-storage of HNTs@NG. In comparison to HNTs and NG shell (Fig. S15), O 1s peak of HNTs@NG shows a significant negative shift, indicating that oxygen of HNTs can attract electron from carbon due to high electronegative of oxygen, creating electron deficiency of NG layer active sites. With the adsorption of K^+, the O 1s (Fig. 5f) peaks shift to lower binding energy compared with pristine HNTs@NG. Considering no obvious shift of the whole Si 2p, Al 2p (Figs. S16 and S17), the shift of O 1s could only derive from the electron density migration from carbon, supposing that K atoms would be stored in the electron deficient carbon rings, and thus, the electron deficiency of carbon atoms in HNTs@NG are more prepared to K-storage than carbon atoms in NG shell.

Based on afore-mentioned the results, it is concluded that the electron deficient state of active sites on N-doped graphene can be obtained after introduction of oxygen by interfacial covalent bonds in heterostructure, which promote the K^+ adsorption and K-storage, improving the electrochemical kinetics and performance. Previous reports focused on the effect of electronic structure on K storage ability of graphene by theoretical simulation. They also have proved that the graphene with electron deficiency can provide K adsorption sites, enhancing the K storage ability [27].

The interfacial structure stability of the cycled HNTs@NG and NG shell were also investigated. After potassiation/depotassiation process,

the HNTs@NG still retains obviously the original 1D tubular morphology (Fig. 5g), possessing a distinct NG layer with 3.3 ± 0.2 nm on HNTs (Fig. 5h). In the case of cycled NG shell sample, the tubular structure is nearly completely deformed (Fig. 5i). This conspicuous difference in morphology implies the fabrication of interfacial framework in heterostructure can tolerate the volume fluctuation of the potassiation/depotassiation, maintaining superior structural integrity. Therefore, the heterostructure not only tailor the electronic structure of active sites, but also improve structure stability.

In order to evaluate the effect of heterogeneous structure on the performance of PIHC, a PIHC device using HNTs@NG and commercial AC as electrodes (denoted as HNTs@NG//AC) is installed, whose discharge process is illustrated in Fig. 6a. The CV curves (from 2.0 to 100 mV s^{-1}) of HNTs@NG//AC show an obvious deformation, which probably derive from the redox reaction of HNTs@NG (Fig. S18). An appropriate operating window of 0.01~4.0 V is selected based on Fig. 6b to estimate the electrochemical behaviors consisting of rate and specific capacity of PIHC devices. As seen in Fig. 6c, the energy density still returns to 72.1 Wh kg^{-1} when the current density switches to 0.1 A g^{-1}, revealing the superb rate of PIHC equipped with HNTs@NG as anode. The nonlinear slopes fitting of HNTs@NG//AC can be observed from GCD curves at various current densities in Fig. 6d, mainly because of a combined energy storage behavior based on HNTs@NG that has

already been confirmed in Fig. 4f. The Ragone plots of HNTs@NG//AC PIHC devices are described in Fig. 6e, which delivers a superior energy density up to 71.5 Wh kg^{-1} at a power density of 214.0 W kg^{-1} in comparison with previously reported other PIHC devices [46–51].

After 2000 cycles, the energy density of PIHC maintains at 49.5 Wh kg^{-1} and 44.5 Wh kg^{-1} under 1.0 A g^{-1} (Fig. 6f) and 2.0 A g^{-1} (Fig. S19), respectively, indicating the conspicuous operating stability. In initial stage, PIHC possesses a low energy density, which is due to the formation of unstable SEI film. According to fitting the results (Fig. S20), the resistance of the surface film on the electrode (R_s) and charge-transfer resistance (R_{ct}) values after 5 cycles for PIHC are 3788 Ω, 1594 Ω, respectively, which is obvious higher than the value after 200 cycles (3005 Ω, 1478 Ω). This indicates that the PIHC owns high resistance and unstable of SEI layer in initial 200 cycles, which confirms that low energy density may be attributed to formation of unstable SEI in initial cycling. In initial stage, SEI layer suffers from intensive mechanical strain that results from K^+ diffusion and transition, causing the unrecoverable cracking, the exfoliation of the relatively fragile SEI layer, the repetitive formation of SEI layers and the excessive consumption of K^+ and electrolyte, thus results in a relative low energy density [52,53]. Finally, to further demonstrate the feasibility of HNTs@NG//AC, the as-fabricated device can power an LED indicator effectively (Fig. 6g), demonstrating its potential for energy storage applications. In further work, the effect of tubular HNTs on electronic structure of carbon based materials should be explored in theory.

4. Conclusions

In order to improve K^+ diffusion and K-storage in graphene, a stable heterogeneous structure by wrapping NG layer on HNTs is successfully fabricated. A series of characteristic results have verified that the formation of covalent bonds between NG layer and HNTs, lead to the electron deficient state in NG layer as active sites, which is beneficial to K^+ diffusion and K-storage. As a result, the achieved specific capacity of HNTs@NG deliver as high as -387.1 mA h g^{-1}, which is markedly higher than that of NG shell and G shell. The K^+ transport kinetic of HNTs@NG also exhibits higher D_K than that of NG shell. Meanwhile, the specific capacity of HNTs@NG maintains 2.2-fold and 4.5-fold higher than that of NG shell and G shell after 2000 cycles at 1.0 A g^{-1}, respectively, which displays high structure stability. The assembled PIHC delivers a high operation working voltage of 4.0 V, an energy density of -72.1 Wh kg^{-1} and cycling stability exceeding 2000 cycles. It is believed that the strategy to fabricate the heterostructure along with the admirable electrochemical performance can pave a novel avenue for the anode electrode of potassium ion energy storage.

CRediT authorship contribution statement

Yongrong Sun: Conceptualization, Methodology, Validation, Formal analysis, Investigation, Writing – review & editing. **Jiefeng Zheng:** Conceptualization, Methodology, Validation, Formal analysis, Investigation. **Fayong Li:** Validation, Formal analysis, Investigation. **Yuanhui Long:** Methodology, Validation, Formal analysis. **Dong Xie:** Conceptualization, Supervision, Project administration, Writing – review & editing. **Hongyan Li:** Conceptualization, Methodology, Formal analysis, Writing – review & editing. **Mingxian Liu:** Conceptualization, Supervision, Project administration, Validation, Writing – review & editing, Funding acquisition.

Declaration of Competing Interest

The authors declare that they have no known competing financial interests or personal relationships that could have appeared to influence the work reported in this paper.

Data availability

Data will be made available on request.

Supplementary materials

Supplementary material associated with this article can be found, in the online version, at doi:10.1016/j.apmt.2022.101702.

References

[1] T. Masese, K. Yoshii, Y. Yamaguchi, T. Okumura, Z.D. Huang, M. Kato, K. Kubota, J. Furutani, Y. Orikasa, H. Senoh, H. Sakaebe, M. Shikano, Rechargeable potassium-ion batteries with honeycomb-layered tellurates as high voltage cathodes and fast potassium-ion conductors, Nat. Commun. 9 (2018) 3823, https://doi.org/10.1038/s41467-018-06343-6.

[2] B.F. Ji, W.J. Yao, Y.P. Zheng, P. Kidkhunthod, X.L. Zhou, S. Tunmee, S. Sattayaporn, H.M. Cheng, H.Y. He, Y.B. Tang, A fluoroxalate cathode material for potassium-ion batteries with ultra-long cyclability, Nat. Commun. 11 (2020) 1225, https://doi.org/10.1038/s41467-020-15044-y.

[3] X. Min, J. Xiao, M.H. Fang, W. Wang, Y.J. Zhao, Y.G. Liu, A.M. Abdelkader, K. Xi, R.V. Kumar, Z.H. Huang, Potassium-ion batteries: outlook on present and future technologies, Energy Environ. Sci. 14 (2021) 2186–2243, https://doi.org/10.1039/D0EE02917C.

[4] Y.J. Wu, Y.J. Sun, Y. Tong, X. Liu, J.F. Zheng, D.X. Han, H.Y. Li, L. Niu, Recent advances in potassium-ion hybrid capacitors: electrode materials, storage mechanisms and performance evaluation, Energy Storage Mater. 41 (2021) 108–132, https://doi.org/10.1016/j.ensm.2021.05.045.

[5] B. Cao, H. Liu, P. Zhang, N. Sun, B. Zheng, Y. Li, H.L. Du, B. Xu, Flexible MXene framework as a fast electron/potassium-ion dual-function conductor boosting stable potassium storage in graphite electrodes, Adv. Funct. Mater. 31 (2021), 2102126, https://doi.org/10.1002/adfm.202102126.

[6] X. Liu, Y.J. Sun, Y. Tong, X.Y. Wang, J.F. Zheng, Y.J. Wu, H.Y. Li, L. Niu, Y. Hou, Exploration in materials, electrolyte and performance towards metal ion (Li, Na, K, Zn and Mg)-based hybrid capacitors: a review, Nano Energy 86 (2021), 106070, https://doi.org/10.1016/j.nanoen.2021.106070.

[7] J.F. Zheng, Y.J. Wu, Y.J. Sun, J.H. Rong, H.Y. Li, L. Niu, Advanced anode materials of potassium ion batteries: from zero dimension to three dimensions, Nano-Micro Lett. 13 (2021) 12, https://doi.org/10.1007/s40820-020-00541-y.

[8] J.M. Wang, B.B. Wang, X.J. Liu, J.T. Bai, H. Wang, G. Wang, Prussian blue analogs (PBA) derived porous bimetal (Mn, Fe) selenide with carbon nanotubes as anode materials for sodium and potassium ion batteries, Chem. Eng. J. 382 (2020), 123050, https://doi.org/10.1016/j.cej.2019.123050.

[9] Z.Q. Tong, R. Yang, S.L. Wu, D. Shen, T.P. Jiao, K.L. Zhang, W.J. Zhang, C.S. Lee, Surface-engineered black niobium oxide@graphene nanosheets for high-performance sodium-/potassium-ion full batteries, Small 15 (2019) 1901272, https://doi.org/10.1002/smll.201901272.

[10] Y.P. Cui, W. Liu, W.T. Feng, Y. Zhang, Y.X. Du, S. Liu, H.L. Wang, M. Chen, J.N. Zhou, Controlled Design of Well-dispersed ultrathin MoS$_2$ nanosheets inside hollow carbon skeleton: toward fast potassium storage by constructing spacious"Houses" for K ions, Adv. Funct. Mater. 30 (2020), 1908755, https://doi.org/10.1002/adfm.201908755.

[11] M.J. Shao, C.X. Li, T. Li, H. Zhao, W.Q. Yu, R.T. Wang, J. Zhang, L.W. Yin, Pushing the energy output and cycling lifespan of potassium-ion capacitor to high level through metal-organic framework derived porous carbon microsheets anode, Adv. Funct. Mater. 30 (2020), 2006561, https://doi.org/10.1002/adfm.202006561.

[12] B.S. Li, B.J. Xi, F.F. Wu, H.Z. Mao, J. Liu, J.K. Feng, S.L. Xiong, One-step in situ formation of N-doped carbon nanosheet 3D porous networks/TiO$_2$ hybrids with ultrafast sodium storage, Adv. Energy Mater. 9 (2019), 1803070, https://doi.org/10.1002/aenm. 201803070.

[13] C.C. Zhang, H.G. Pan, L.X. Sun, F. Xu, Y.F. Ouyang, F. Roseid, Progress and perspectives of 2D materials as anodes for potassium-ion batteries, Energy Storage Mater. 38 (2021) 354–378, https://doi.org/10.1016/j.ensm.2021.03.007.

[14] R. Tao, F. Li, X. Lu, F. Liu, J.H. Xu, D.J. Kong, C. Zhang, X.Y. Tan, S.X. Ma, W. Y. Shi, R.W. Mo, Y.F. Lu, High-conductivity-dispersibility graphene made by catalytic exfoliation of graphite for lithium-ion battery, Adv. Funct. Mater. 31 (2021), 2007630, https://doi.org/10.1002/adfm.202007630.

[15] Z.M. Liu, J. Wang, X.X. Jia, W.L. Li, Q.F. Zhang, L. Fan, H.B. Ding, H.G. Yang, X. Z. Yu, X.K. Li, B.G. Lu, Graphene armored with a crystal carbon shell for ultrahigh-performance potassium ion batteries and aluminum batteries, ACS Nano 13 (2019) 10631–10642, https://doi.org/10.1021/acsnano.9b04893.

[16] S. Gong, Q. Wang, Boron-doped graphene as a promising anode material for potassium-ion batteries with a large capacity, high rate performance, and good cycling stability, J. Phys. Chem. C 121 (2017) 24418–24424, https://doi.org/10.1021/acs.jpcc.7b07583.

[17] Y. Zhao, J.J. Zhu, S.J.H. Ong, Q.Q. Yao, X.L. Shi, K. Hou, Z.J. Xu, L.H. Guan, High-rate and ultralong cycle-life potassium ion batteries enabled by in situ engineering of yolk-shell FeS$_2$@C structure on graphene matrix, Adv. Energy Mater. 8 (2018), 1802565, https://doi.org/10.1002/aenm.201802565.

[18] C. Shen, G.Q. Song, X.L. Zhu, D. Wang, L. Huang, Z.H. Sun, Y.P. Wu, An in-depth study of heteroatom boosted anode for potassium-ion batteries, Nano Energy 78 (2020), 105294, https://doi.org/10.1016/j.nanoen.2020.105294.

[19] Z.H. Chen, X.H. An, L.M. Dai, Y.X. Xu, Holey graphene-based nanocomposites for efficient electrochemical energy storage, Nano Energy 73 (2020), 104762, https://doi.org/10.1016/j.nanoen.2020.104762.

[20] H.Y. Li, Z. Cheng, A. Natan, A.M. Hafez, D.X. Cao, Y. Yang, H.L. Zhu, Dual function, tunable, nitrogen doped carbon for high performance Li metal-sulfur full cell, Small 15 (2019), 1804609, https://doi.org/10.1002/smll.201804609.

[21] C.J. Chen, Z.G. Wang, B. Zhang, L. Miao, J. Cai, L.F. Peng, Y.Y. Huang, J.J. Jiang, Y.H. Huang, L.N. Zhang, J. Xie, Nitrogen-rich hard carbon as a highly durable anode for high-power potassium-ion batteries, Energy Storage Mater. 8 (2017) 161–168, https://doi.org/10.1016/j.ensm.2017.05.010.

[22] S. Tao, W. Xu, J.H. Zheng, F.J. Kong, P.X. Cui, D.J. Wu, B. Qian, S.M. Chen, L. Song, Soybean roots-derived N, P Co-doped mesoporous hard carbon for boosting sodium and potassium-ion storage, Carbon 178 (2021) 233–242, https://doi.org/10.1016/j.carbon.2021.03.022.

[23] Z.C. Ju, S. Zhang, Z. Xing, Q.C. Zhuang, Y.H. Qiang, Y.T. Qian, Direct synthesis of few-layer F-doped graphene foam and its lithium/potassium storage properties, ACS Appl. Mater. Interfaces 8 (2016) 20682–20690, https://doi.org/10.1021/acsami. 6b04763.

[24] M. Chen, W. Wang, X. Liang, S. Gong, J. Liu, Q. Wang, S.J. Guo, H. Yang, Sulfur/oxygen codoped porous hard carbon microspheres for high-performance potassium-ion batteries, Adv. Energy Mater. 8 (2018), 1800171, https://doi.org/10.1002/aenm.201800171.

[25] Y. Liu, H.D. Dai, L. Wu, W.B. Zhou, L. He, W.G. Wang, W.Q. Yan, Q.H. Huang, L. J. Fu, Y.P. Wu, A large scalable and low-cost sulfur/nitrogen dual doped hard carbon as the negative electrode material for high-performance potassium-ion batteries, Adv. Energy Mater. 9 (2019), 1901379, https://doi.org/10.1002/aenm.201901379.

[26] K. Share, A.P. Cohn, R. Carter, B. Rogers, C.L. Pint, Role of nitrogen doped graphene for improved high capacity potassium ion battery anodes, ACS Nano 10 (2016) 9738–9744, https://doi.org/10.1021/acsnano.6b05998.

[27] Y. Xu, C.L. Zhang, M. Zhou, Q. Fu, C.X. Zhao, M.H. Wu, Y. Lei, Highly nitrogen doped carbon nanofibers with superior rate capability and cyclability for potassium ion batteries, Nat. Commun. 9 (2018) 1720, https://doi.org/10.1038/s41467-018-04190-z.

[28] X.Y. Lian, J.H. Zhou, Y.Z. You, Z.N. Tian, Y.Y. Yi, J.H. Choi, M.H. Rümmeli, J. Y. Sun, Boosting K$^+$ capacitive storage in dual-doped carbon crumples with B-N moiety via a general protic-salt synthetic strategy, Adv. Funct. Mater. 32 (2022), 2109969, https://doi.org/10.1002/adfm.202109969.

[29] X.Y. Lian, Z.T. Sun, Q.Q. Mei, Y.Y. Yi, J.H. Zhou, M.H. Rümmeli, J.Y. Sun, Biomass template derived boron/oxygen Co-doped carbon particles as advanced anodes for potassium-ion batteries, Energy Environ. Mater. 5 (2022) 344–352, https://doi.org/10.1002/eem2.12183.

[30] R.A. Adams, J.M. Syu, Y.P. Zhao, C.T. Lo, A. Varma, V.G. Pol, Binder-Free N- and O-rich carbon nanofiber anodes for long cycle life K-ion batteries, ACS Appl. Mater. Interfaces 9 (2017) 17872–17881, https://doi.org/10.1021/acsami.7b02476.

[31] X.J. Zhao, C.R. Zhou, Y. Lvov, M.X. Liu, Clay nanotubes aligned with shear forces for mesenchymal stem cell patterning, Small 15 (2019), 1900357, https://doi.org/10.1002/smll.201900357.

[32] V. Bertolino, G. Cavallaro, S. Milioto, G. Lazzara, Polysaccharides/Halloysite nanotubes for smart bionanocomposite materials, Carbohyd. Polym. 254 (2020), 116502, https://doi.org/10.1016/j.carbpol.2020.116502.

[33] A. Glotov, A. Vutolkina, A. Pimerzin, V. Vinokurov, Y. Lvov, Clay nanotube-metal core/shell catalysts for hydroprocesses, Chem. Soc. Rev. 50 (2021) 9240–9277, https://doi.org/10.1039/D1CS00502B.

[34] L. Lisuzzo, G. Cavallaro, S. Milioto, G. Lazzara, Halloysite nanotubes as nanoreactors for heterogeneous micellar catalysis, J. Colloid. Interf. Sci. 608 (2022) 424–434, https://doi.org/10.1016/j.jcis.2021.09.146.

[35] Y.J. Wu, J.F. Zheng, Y. Tong, X. Liu, Y.J. Sun, L. Niu, H.Y. Li, Carbon hollow tube confined Sb/Sb$_2$S$_3$ nanorod fragments as a highly stable anode for potassium ion batteries, ACS Appl. Mater. Interfaces 13 (2021) 51066–51077, https://doi.org/10.1021/acsami.1c16267.

[36] X. Hu, Y.J. Liu, J.X. Chen, L.C. Yi, H.B. Zhan, Z.H. Wen, Fast redox kinetics in Bi-heteroatom doped 3D porous carbon nanosheets for high-performance hybrid potassium-ion battery capacitors, Adv. Energy Mater. 9 (2019), 1901533, https://doi.org/10.1002/aenm.201901533.

[37] D.P. Li, X.H. Ren, Q. Ai, Q. Sun, L. Zhu, Y. Liu, Z. Liang, R.Q. Peng, P.C. Si, J. Lou, J. K. Feng, L.J. Ci, Facile fabrication of nitrogen-doped porous carbon as superior anode material for potassium-ion batteries, Adv. Energy Mater. 8 (2018), 1802386, https://doi.org/10.1002/aenm.201802386.

[38] P. Yuan, D.Y. Tan, F. Annabi-Bergaya, W.C. Yan, M.D. Fan, D. Liu, H.P. He, Changes in structure, morphology, porosity, and surface activity of mesoporous halloysite nanotubes under heating, Clay, Clay Miner 60 (2012) 561–573, https://doi.org/10.1346/CCMN.2012.0600602.

[39] P.X. Xiong, P.X. Bai, S.B. Tu, M.R. Cheng, J.F. Zhang, J. Sun, Y.H. Xu, Red phosphorus nanoparticle@3D interconnected carbon nanosheet framework composite for potassium-ion battery anodes, Small 14 (2018), 1802140, https://doi.org/10.1002/smll.201802140.

[40] K. Share, A.P. Cohn, R. Carter, C.L. Pint, Role of nitrogen-doped graphene for improved high-capacity potassium ion battery anodes, ACS Nano 10 (2016) 9738–9744, https://doi.org/10.1021/acsnano.6b05998.

[41] X.H. Zhang, D.H. Wang, X.Y. Qiu, Y.J. Ma, D.B. Kong, K. Müllen, X.L. Li, L.J. Zhi, Stable high-capacity and high-rate silicon-based lithium battery anodes upon two-dimensional covalent encapsulation, Nat. Commun. 11 (2020) 3826, https://doi.org/10.1038/s41467-020-17686-4.

[42] L. David, R. Bhandavat, U. Barrera, G. Singh, Silicon oxycarbide glass-graphene composite paper electrode for long-cycle lithium-ion batteries, Nat. Commun. 7 (2016) 10998, https://doi.org/10.1038/ncomms10998.

[43] H.N. He, D. Huang, Y.G. Tang, Q. Wang, X.B. Ji, H.Y. Wang, Z.P. Guo, Tuning nitrogen species in three-dimensional porous carbon via phosphorus doping for ultra-fast potassium storage, Nano Energy 57 (2019) 728–736, https://doi.org/10.1016/j.nanoen.2019.01.009.

[44] W. Wang, J.H. Zhou, Z.P. Wang, L.Y. Zhao, P.H. Li, Y. Yang, C. Yang, H.X. Huang, S.J. Guo, Short-range order in mesoporous carbon boosts potassium-ion battery performance, Adv. Energy Mater. 8 (2018), 1701648, https://doi.org/10.1002/aenm.201701648.

[45] Y. Liu, Y.X. Lu, Y.S. Xu, Q.S. Meng, J.C. Gao, Y.G. Sun, Y.S. Hu, B.B. Chang, C. T. Liu, A.M. Cao, Pitch-derived soft carbon as stable anode material for potassium ion batteries, Adv. Mater. 32 (2020), 2000505, https://doi.org/10.1002/adma.202000505.

[46] M. Moussa, S.A. Al-Bataineh, D. Losic, D.P. Dubal, Engineering of high-performance potassium-ion capacitors using polyaniline-derived N-doped carbon nanotubes anode and laser scribed graphene oxide cathode, Appl. Mater. Today 16 (2019) 425–434, https://doi.org/10.1016/j.apmt.2019.07.003.

[47] S.Y. Dong, Z.F. Li, Z.Y. Xing, X.Y. Wu, X.L. Ji, X.G. Zhang, Novel potassium-ion hybrid capacitor based on an anode of K$_2$Ti$_6$O$_{13}$ microscaffolds, ACS Appl. Mater. Interfaces 10 (2018) 15542–15547, https://doi.org/10.1021/acsami.7b15314.

[48] H.V. Ramasamy, B. Senthilkumar, P. Barpanda, Y.S. Lee, Superior potassium-ion hybrid capacitor based on novel P3-type layered K$_{0.45}$Mn$_{0.5}$Co$_{0.5}$O$_2$ as high capacity cathode, Chem. Eng. J. 368 (2019) 235–243, https://doi.org/10.1016/j.cej.2019.02.172.

[49] S.Q. Zhao, L.B. Dong, B. Sun, K. Yan, J.Q. Zhang, S.W. Wan, F.R. He, P. Munroe, P. H.L. Notten, G.X. Wang, K$_2$Ti$_2$O$_5$@C microspheres with enhanced K$^+$ intercalation pseudocapacitance ensuring fast potassium storage and long-term cycling stability, Small 16 (2020), 1906131, https://doi.org/10.1002/smll.201906131.

[50] F.B. Huang, W.P. Liu, Q.Y. Wang, F. Wang, Q.R. Yao, D.L. Yan, H.R. Xu, B.Y. Xia, J. Q. Deng, Natural N/O-doped hard carbon for high performance K-ion hybrid capacitors, Electrochim. Acta 354 (2020) 136701, https://doi.org/10.1016/j.electacta.2020.136701.

[51] L. Zhou, M.Y. Zhang, Y.F. Wang, Y.S. Zhu, L.J. Fu, X. Liu, Y.P. Wu, W. Huang, Cubic prussian blue crystals from a facile one-step synthesis as positive electrode material for superior potassium-ion capacitors, Electrochim. Acta 232 (2017) 106–113, https://doi.org/10.1016/j.electacta.2017.02.096.

[52] A.J. Naylor, M. Carboni, M. Valvo, R. Younesi, Interfacial reaction mechanisms on graphite anodes for K-ion batteries, ACS Appl. Mater. Interfaces 11 (2019) 45636–45645, https://doi.org/10.1021/acsami.9b15453.

[53] B. Wang, F. Yuan, W. Li, Q.J. Wang, X.M. Ma, L. Gu, H.L. Sun, K. Xi, D. Zhang, W. Wang, Rational formation of solid electrolyte interface for high-rate potassium ion batteries, Nano Energy 75 (2020), 104979, https://doi.org/10.1016/j.nanoen.2020.104979.

Supplementary Materials

Halloysite Nanotube@N-doped Graphene Heterostructure Enabled Advanced Potassium Ion Hybrid Capacitor Anode

Yongrong Sun[a], Jiefeng Zheng[b], Fayong Li[a], Yuanhui Long[b], Dong Xie[a]*, Hongyan Li[b]**, Mingxian Liu[b]***

[a] Biomaterials Engineering Technology Research Center, Institute of Biological and Medical Engineering, Guangdong Academy of Sciences, Guangzhou 510316, China
[b] Department of Materials Science and Engineering, College of Chemistry and Materials Science, Jinan University, Guangzhou 511443, China

* Corresponding author. E-mail: xd0929@163.com (Dong Xie)
** Corresponding author. E-mail: lihongyan@jnu.edu.cn (Hongyan Li)
*** Corresponding author. E-mail: liumx@jnu.edu.cn (Mingxian Liu)
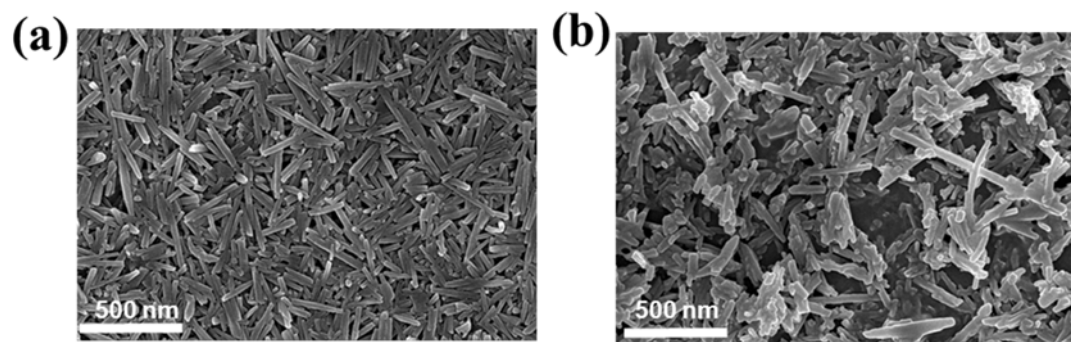
Fig. S1. SEM images of (a) HNTs and (b) HNTs@NG.
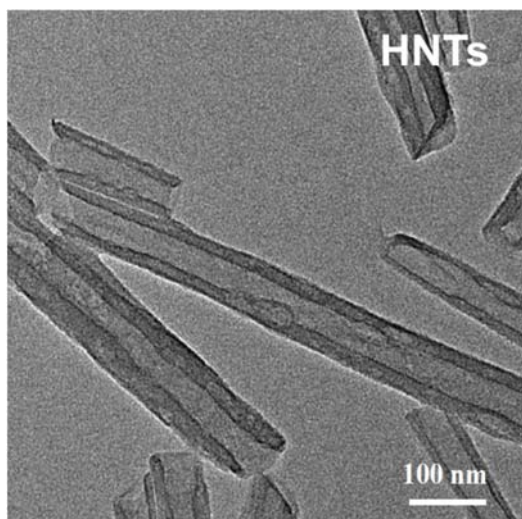
Fig. S2. TEM of HNTs.
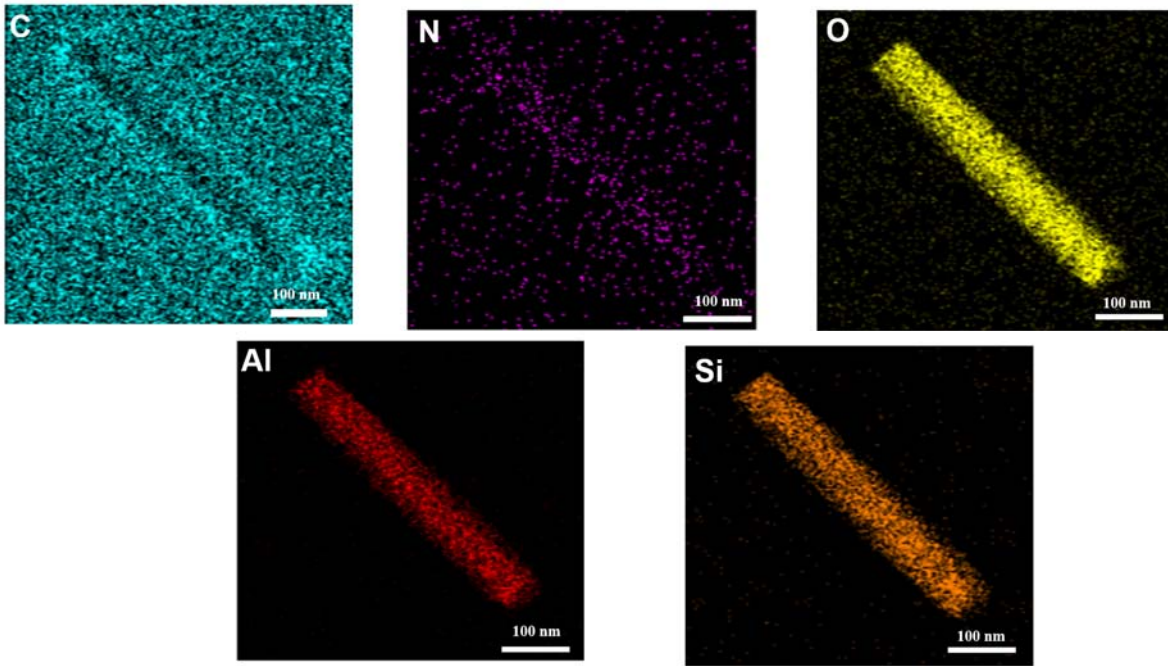
Fig. S3. Elemental mappings of HNTs@NG.
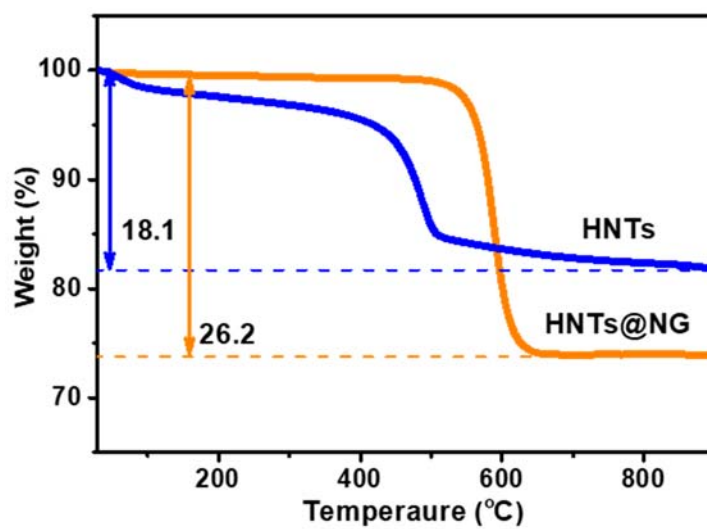
Fig. S4. TG curves of HNTs and HNTs@NG.
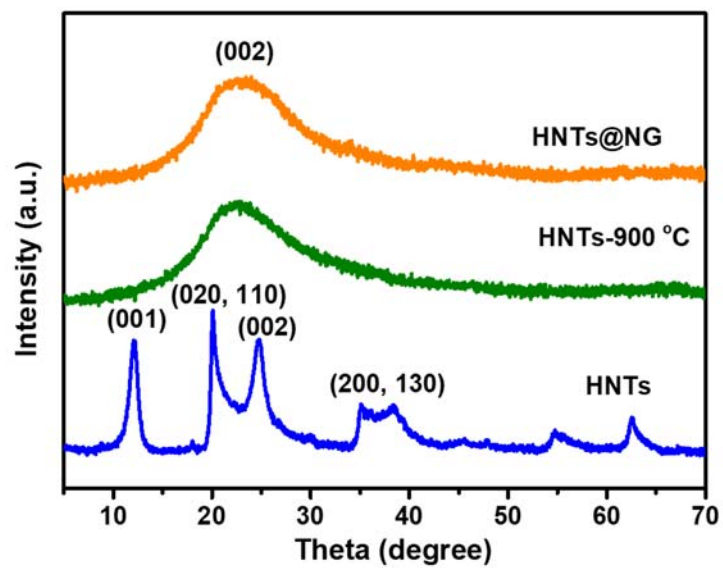
Fig. S5. XRD patterns of HNTs, HNTs-900℃ and HNTs@NG.
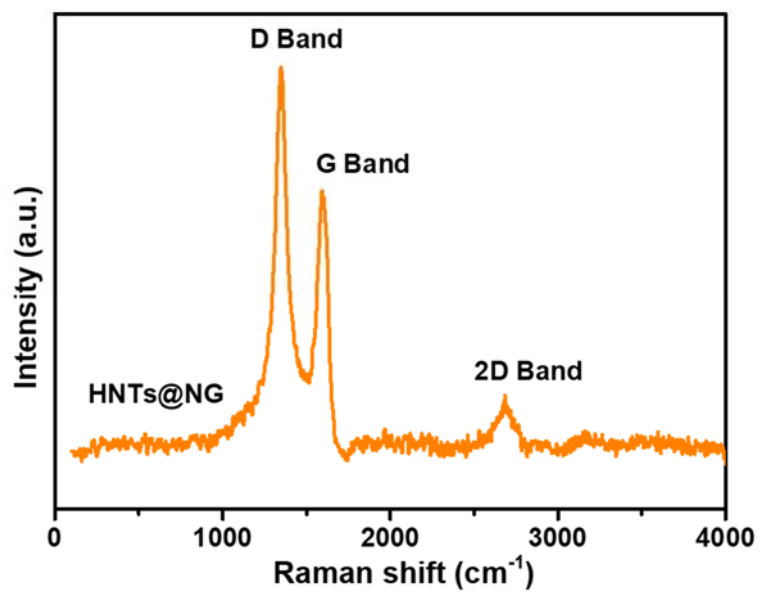
Fig. S6. Raman spectrum of HNTs@NG.
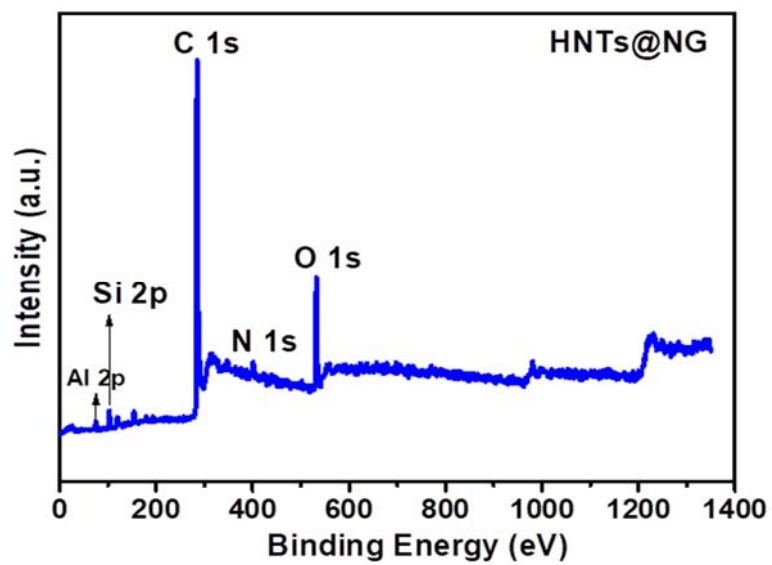
Fig. S7. XPS spectra of HNTs@NG.
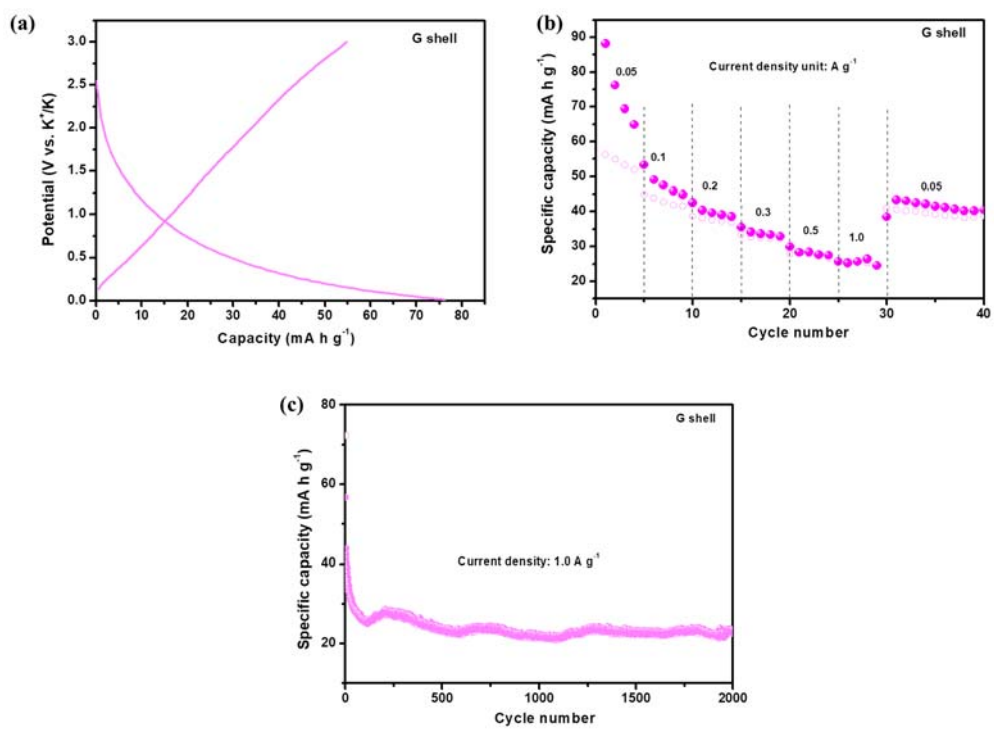
Fig. S8. Electrochemical performance of G shell, (a) GCD curves at 0.05 A g^{-1}, (b) rate performance, (c) long-term cycling performance under current densities of 1.0 A g^{-1}.
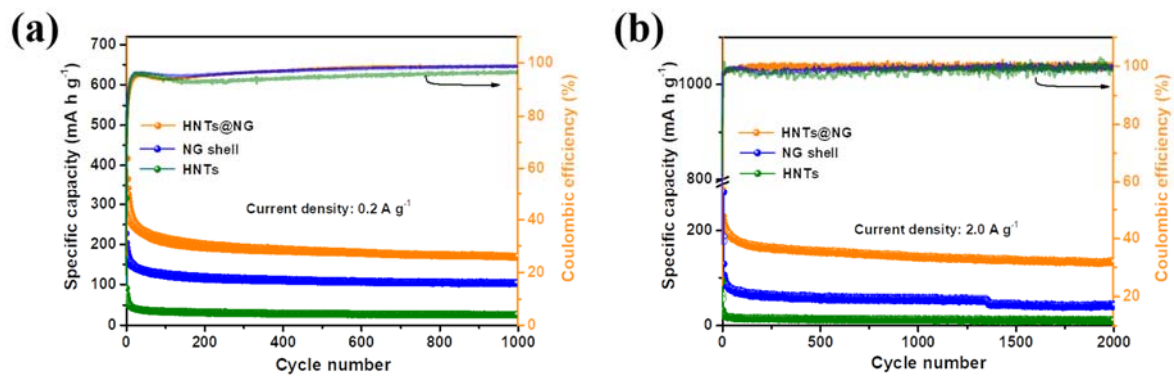
Fig. S9. Long-term cycling performance of HNTs@NG, HNTs and NG shell under current densities of 0.2 A g^{-1} (a) and 2.0 A g^{-1} (b).
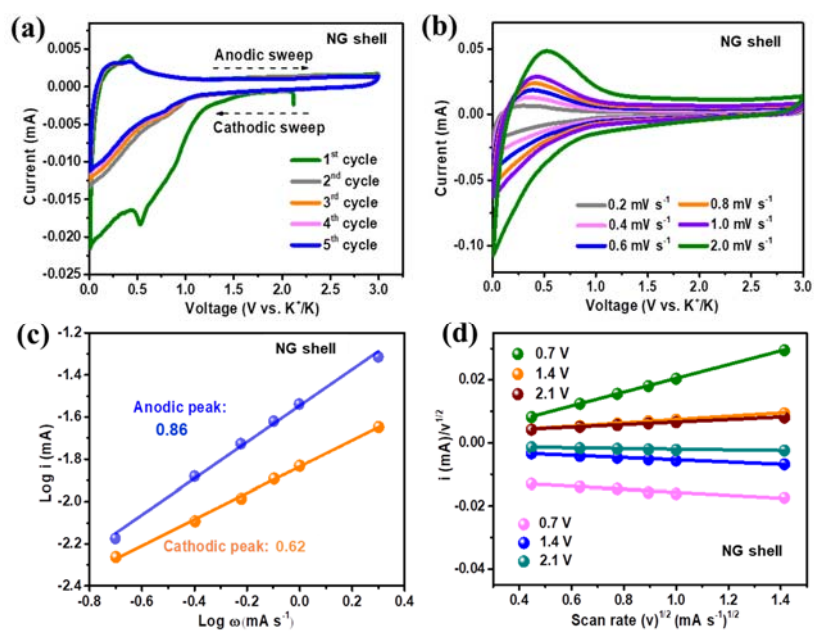
Fig. S10. Electrochemical kinetic analysis of potassium ions storage behavior of NG shell. (a) CV curves (first to fifth cycles) at the scan rate of 0.1 mV s^{-1}, (b) CV curves obtained at the scan rate of 0.2, 0.4, 0.6, 0.8, 1.0, 2.0 mV s^{-1}, (c) the plots of log (i) vs. log(ω), (d) Relationship between i/v$^{1/2}$ vs. v$^{1/2}$ used to obtained k_1 and k_2.
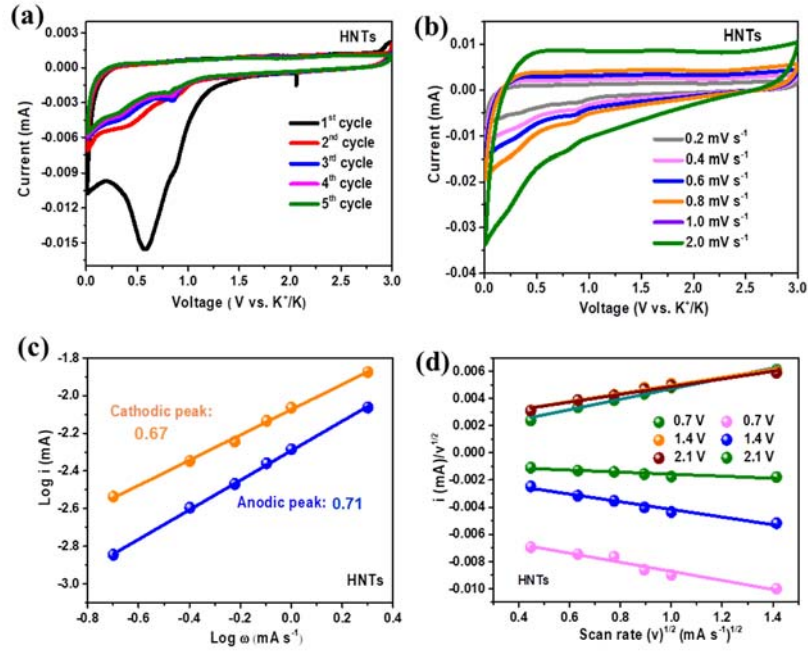
Fig. S11. Electrochemical kinetic analysis of potassium ions storage behavior of HNTs.(a) CV curves (first to fifth cycles) at the scan rate of 0.1 mV s^{-1}, (b) CV curves obtained at the scan rate of 0.2, 0.4, 0.6, 0.8, 1.0, 2.0 mV s^{-1}, (c) the plots of log (i) vs. log(ω), (d) Relationship between i/v$^{1/2}$ vs. v$^{1/2}$ used to obtained k_1 and k_2.
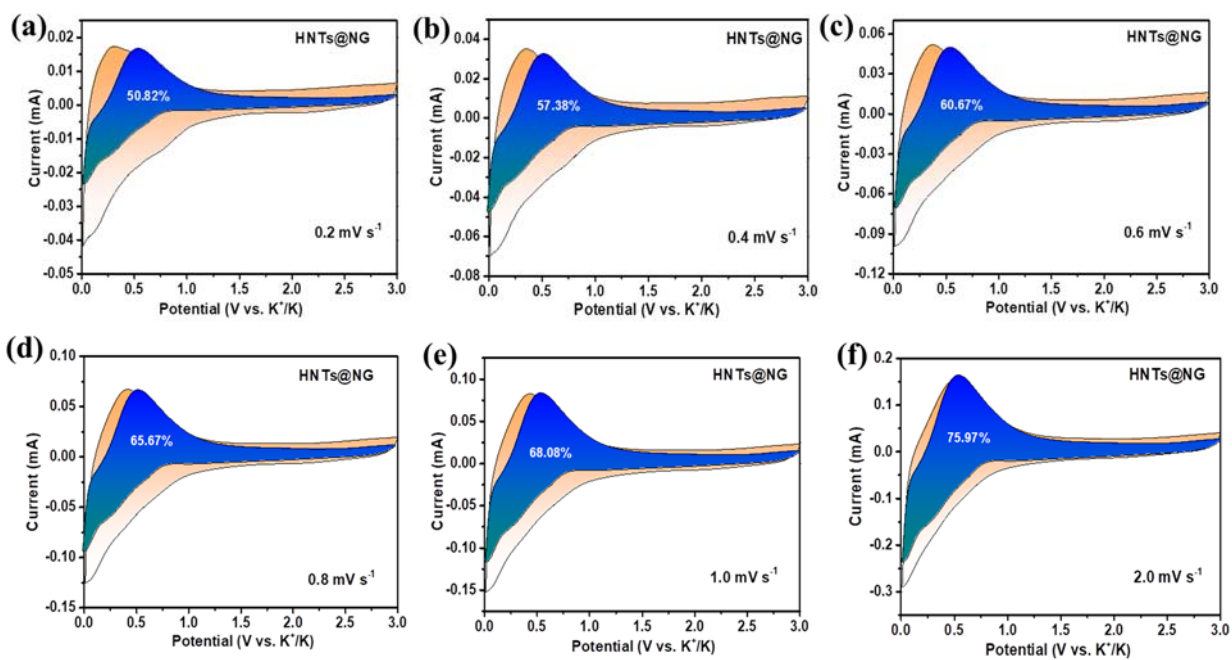
Fig. S12. Contribution ratios of capacities and diffusion capacities at various scan rates for HNTs@NG.
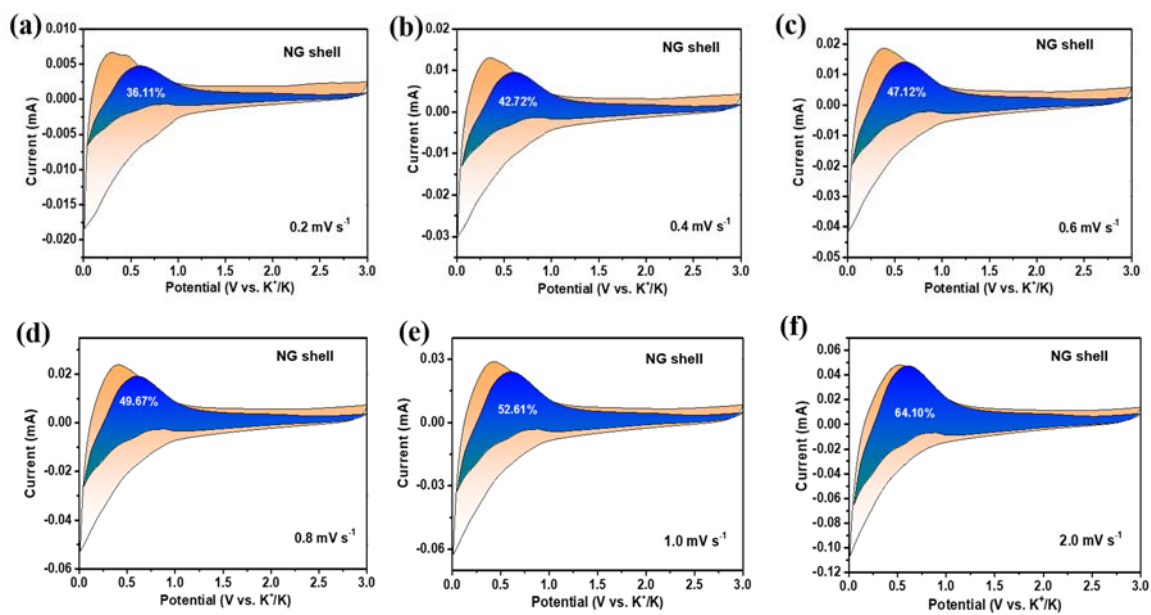
Fig. S13. Contribution ratios of capacities and diffusion capacities at various scan rates of NG shell.
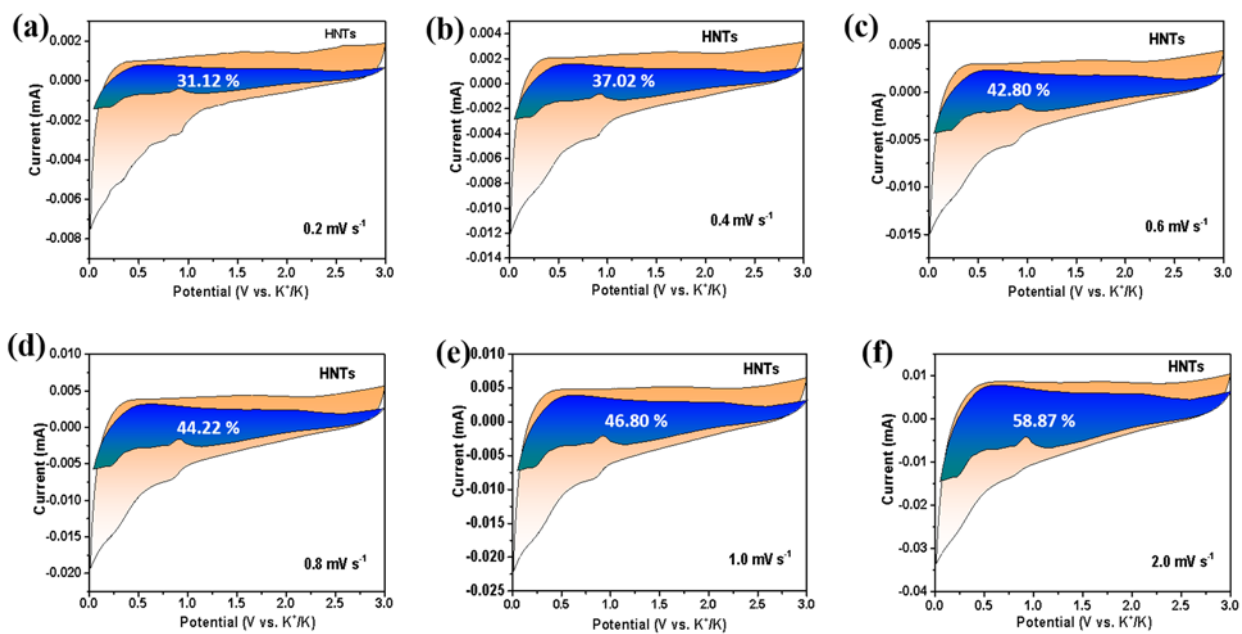
Fig. S14. Contribution ratios of capacities and diffusion capacities at various scan rates of HNTs.
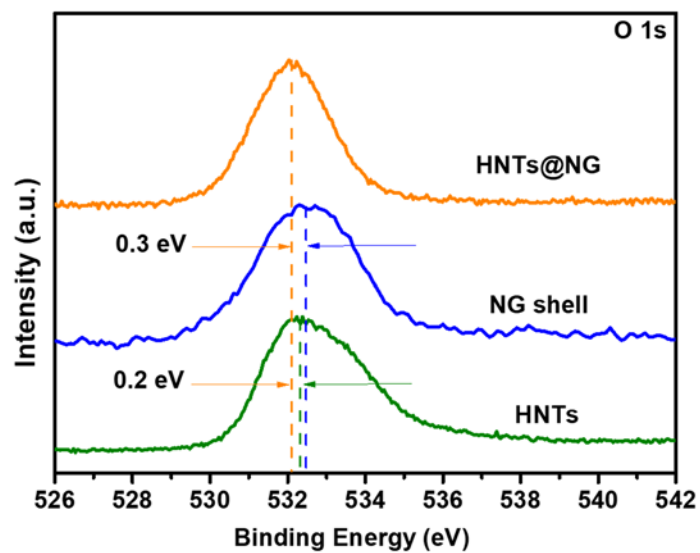
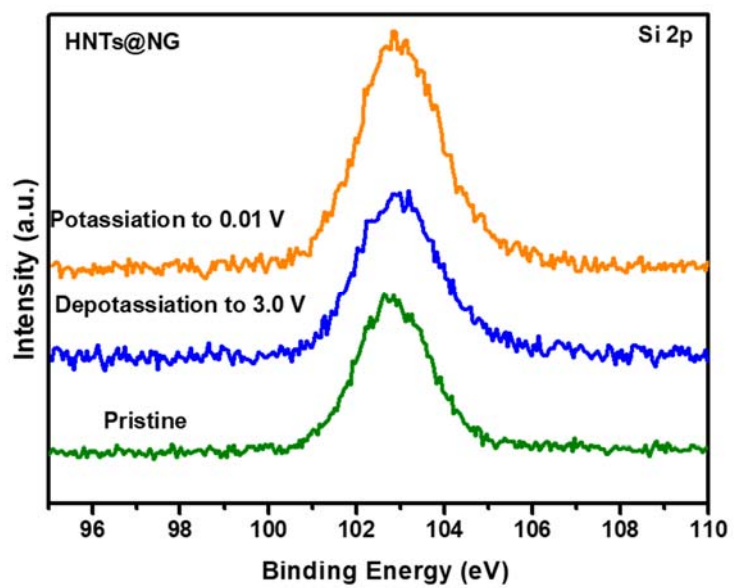**Fig. S15.** O 1s spectra spectra of HNTs@NG, NG shell and HNTs.

Fig. S16. Si 2p spectra spectra of HNTs@NG under potassiation/depotassiation at 1.0 A g^{-1}.
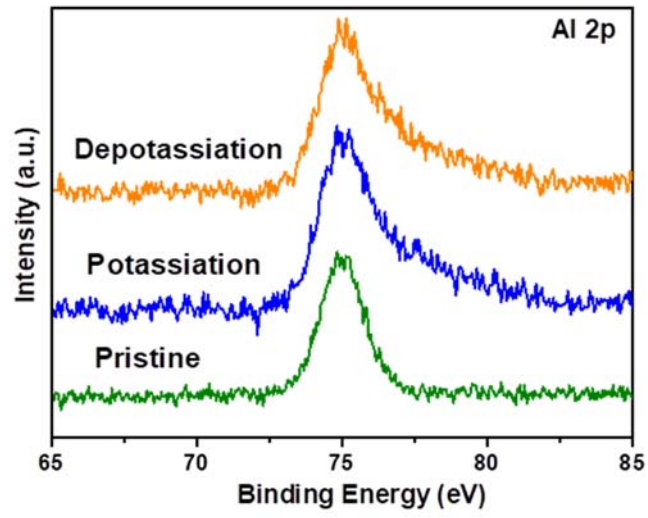
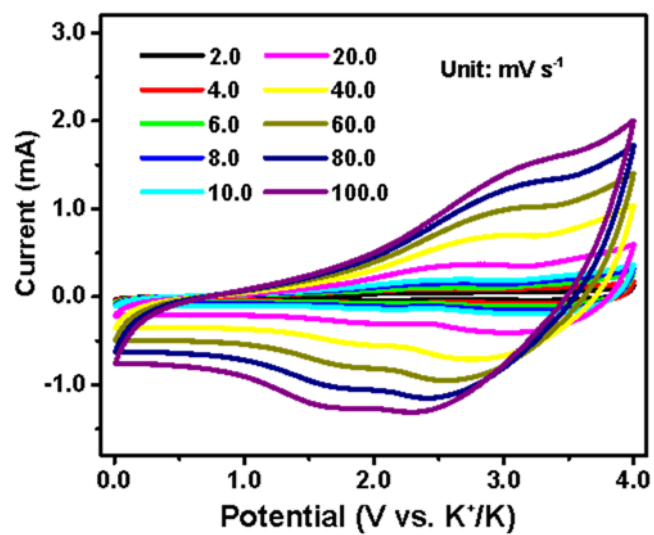**Fig. S17.** Al 2p spectra spectra of HNTs@NG under potassiation/depotassiation at 1.0 A g^{-1}.

Fig. S18. CV curves of HNTs@NG//AC potassium ion hybrid capacitor obtained at the scan rate of 2.0, 4.0, 6.0, 8.0, 10.0, 20.0, 40.0, 60.0, 80.0,100.0 mV s^{-1}.
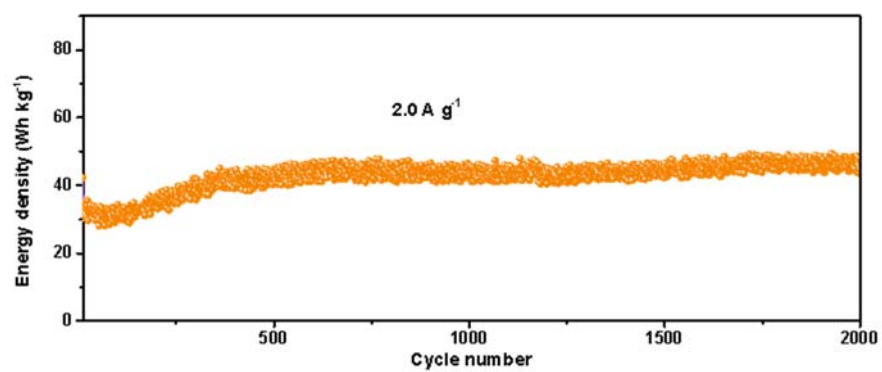
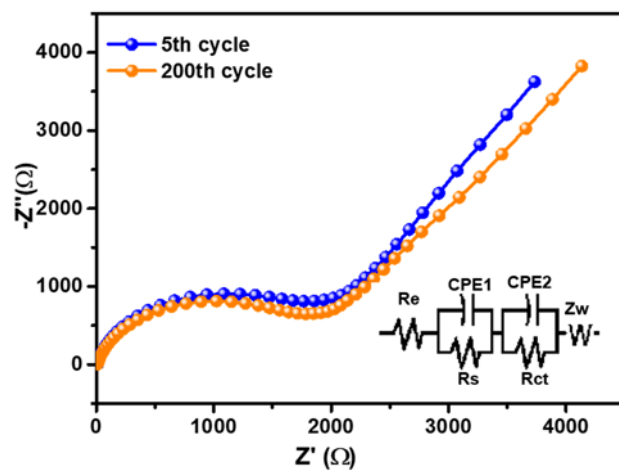**Fig. S19.** Long-term cyclic performance of the HNTs@NG//AC hybrid capacitor device at 2.0 A g^{-1}.

Fig. S20. Nyquist plot of the 5th and 200th cycles and equivalent circuit (inset) of PIHC.

R_e is the electrolyte resistance, CPE1 and R_s are the capacitance and resistance of the surface film on the electrode respectively. CPE2 and R_{ct} are the double layer capacitance and charge-transfer resistance, respectively. Z_w is the Warburg impedance related to the diffusion of K^+ ion into the bulk electrode.